The Importance of Aerosol and Droplet Microphysics for the Properties and Life Cycle of Radiation Fog in the Po Valley

Hao Ding[1,2], Almuth Neuberger[2,3], Rahul Ranjan[2,3], Fredrik Mattsson[2,3], Liine Heikkinen[2,3], Karam Mansour[4], Stefano Decesari[4], Claudia Mohr[2,3,5,6], Alejandro Baró Pérez[1,2], Nazario Mastroianni[1,2,3], Paul Zieger[2,3], Ilona Riipinen[2,3], and Annica M. L. Ekman[1,2]

[1]Department of Meteorology, Stockholm University, Stockholm, Sweden
[2]Bolin Centre for Climate Research, Stockholm, Sweden
[3]Department of Environmental Science, Stockholm University, Stockholm, Sweden
[4]Institute of Atmospheric Science and Climate, National Research Council of Italy, Bologna, Italy
[5]now at: Center for Energy and Environmental Sciences, Paul Scherrer Institute, Villigen, Switzerland
[6]now at: Department of Environmental Systems Science, ETH Zurich, Zurich, Switzerland

Correspondence: Hao Ding (hao.ding@misu.su.se) and Annica M. L. Ekman (annica.ekman@misu.su.se)

Abstract. Employing high-resolution Large Eddy Simulation (LES) coupled with interactive aerosol and cloud microphysics schemes, this study investigates the influence of aerosol and droplet microphysics on the life cycle and properties of wintertime radiation fog in the Po Valley, Italy. For the simulated case, the results show that the main drivers of radiation fog onset and dissipation are nocturnal longwave cooling and surface warming, respectively. Increasing aerosol loading increases droplet
5 number concentration, liquid water content, and fog optical thickness, which reduces droplet sedimentation rates and prolongs fog duration by up to 54 minutes. Overall, the microphysical influence of aerosols and droplets weakens under heavily polluted conditions. We also show that non-activated hydrated aerosols have a limited influence on total liquid water content and fog-layer mixing. However, they critically affect visibility and fog duration prediction, underscoring the importance of explicitly incorporating hydrated particles in fog forecasting and accurately representing aerosol composition. Additional sensitivity
10 experiments reveal that the prescribed droplet spectral shape parameters significantly influence fog characteristics. Parameter settings that represent a broad droplet size spectrum overestimate the number of large droplets compared to observations, which increases mean droplet sedimentation rates and decreases mean liquid water content by up to 104% and 78%, respectively, compared to the settings that best represent the observed spectrum.

1 Introduction

15 Fog is a common phenomenon in the atmospheric boundary layer, posing significant risks to transportation safety and public health due to low visibility and the accumulation of pollutants. Prolonged fog events can also adversely affect crop growth and agricultural productivity, leading to reduced yields. (Gultepe et al., 2007; Decesari et al., 2017; Leung et al., 2020; Bergot and Koracin, 2021; Lakra and Avishek, 2022). Radiation fog, one of the most frequent types of fog over land, forms primarily due to nocturnal surface radiative cooling, which leads to water vapor supersaturation and droplet formation. As the fog
20 thickens, longwave radiative cooling at the fog top increases, promoting further condensation, while also inducing fog layer

mixing through turbulence. The fog dissipation process is typically dominated by near-surface warming induced by shortwave radiation at sunrise, as well as turbulent entrainment of dry air at the fog top, reducing relative humidity and causing droplet evaporation (Gultepe et al., 2007; Bergot, 2013; Wainwright et al., 2021). Overall, the evolution of radiation fog is governed by a complex interplay of thermodynamic, dynamic, and microphysical processes in the boundary layer. These processes,

25   including radiation, turbulent mixing, aerosol–droplet interactions, and surface exchange, are highly coupled yet nonlinear, making fog simulation and forecasting challenging (Gultepe et al., 2007; Haeffelin et al., 2010; Maronga and Bosveld, 2017; Mazoyer et al., 2019).

High-resolution large-eddy simulation (LES) models are useful tools for studying boundary-layer processes, including radiation fog, since they explicitly resolve large-scale turbulent eddies and represent supersaturation dynamics better than typical

30   weather forecast and climate models. When coupled with radiation and aerosol–cloud microphysics schemes, LES models have been shown to represent the aforementioned nonlinear interactions and the life cycle of radiation fog reasonably well. LES has been used extensively to investigate the sensitivity of fog to meteorological conditions (e.g., surface forcing and advection) as well as aerosol properties (e.g., number concentration) (Bergot, 2013; Stolaki et al., 2015; Maalick et al., 2016). Nevertheless, the representation of aerosol-droplet-fog interactions remains one of the major uncertainties in the simulations (Boutle et al.,

35   2022).

As a substrate for water vapor condensation, the hygroscopic growth and activation of aerosol particles are crucial for droplet formation. Previous modeling studies of aerosol-fog interactions have shown that higher aerosol number concentrations result in more activated droplets, increased liquid water content (LWC), and an optically thicker fog, which delays fog dissipation and thereby prolongs fog lifetime (Bott et al., 1990; Zhang et al., 2014; Stolaki et al., 2015; Maalick et al., 2016). Furthermore,

40   non-activated hydrated aerosols, having grown to micron sizes, can also influence the optical properties of fog. These hydrated particles remain relatively small and have little effect on the longwave radiation budget and the optical thickening of fog (Boutle et al., 2018). However, due to their large number and high scattering and extinction efficiency, hydrated particles can substantially reduce visibility, even in the absence of activated droplets (Kokkola et al., 2003; Elias et al., 2009; Hammer et al., 2014; Elias et al., 2015). The ability of dry aerosol particles to take up water can be expressed by the hygroscopicity parameter

45   (κ), which depends on the chemical composition and mixing state of the aerosol (Petters and Kreidenweis, 2007). Under highly polluted conditions, intense competition for water vapor due to the abundance of cloud condensation nuclei (CCN) leads to low ambient supersaturation values, which limits the number of activated fog droplets. Thus, in polluted environments and in relation to the size distribution, the chemical composition and hygroscopicity of aerosols have been suggested to play a limited role in droplet activation and fog processes (Bott, 1991; Mazoyer et al., 2019; Neuberger et al., 2025a). In contrast, under clean

50   conditions and with higher supersaturation values, a larger fraction of hydrated particles is closer to the critical activation size, and the κ value would play a larger role for the number of droplets activated.

The shape of the droplet size distribution is also important for fog evolution, as it describes the distribution of LWC across droplets as well as the relationship between LWC and the droplet number concentration N_c (Mazoyer et al., 2022). For a droplet spectrum that follows a gamma distribution and a given N_c, larger shape parameters (i.e., α and ν in Sect. S1 in

55   the Supplementary Information) yield a narrower droplet spectrum, which typically suppresses autoconversion and sustains

higher droplet number concentrations (Seifert and Beheng, 2001). Moreover, a narrow size distribution reduces the effective droplet radius, a key factor determining cloud and fog optical properties (Morrison and Grabowski, 2007). Previous studies have demonstrated that variations in droplet size distribution parameterizations can influence key fog processes, including collision-coalescence efficiency, sedimentation rates, and the vertical extent of the fog layer (Boutle et al., 2022; Pope and Igel, 2023). In previous numerical studies, shape parameters are often empirically prescribed based on the geographical region (e.g., Bari et al., 2015; Wurtz et al., 2021; Contreras Osorio et al., 2022), an idealized practice that limits their general applicability. Notably, even within a single fog event, shape parameters exhibit considerable variability, with local values showing no clear correlation with droplet number concentrations (Miles et al., 2000; Geoffroy et al., 2010; Igel and van den Heever, 2017). Despite the substantial uncertainties, there have been only a few numerical studies that examined how the fog life cycle is affected by the representation of the droplet size distribution.

In this study, we make use of LES and an extensive dataset of fog properties from the Fog and Aerosol Interaction Research Italy (FAIRARI) field campaign 2021/22 in the Po Valley (Neuberger et al., 2025b) to examine aerosol-fog interactions from a microphysical perspective. The FAIRARI dataset includes meteorological conditions, aerosol physicochemical properties, and droplet measurements, providing a basis for model initialization and serving as a reference for model evaluation. The dataset encompasses detailed information on the size distribution of aerosols and cloud droplets, making it particularly suitable for investigating fog microphysical features. The Po Valley is in general an interesting area for aerosol-fog interaction studies – it is a region of frequent radiation fog formation, and several field campaigns focusing on fog have been carried out there in the past (e.g., Fuzzi et al., 1992; Frank et al., 1998; Hamed et al., 2007; Decesari et al., 2017; Paglione et al., 2020). Furthermore, pollution levels today are much lower than in the 1980s (cf. Noone et al., 1992), which may influence the life cycle and properties of the fog. Despite the lower pollution levels, Neuberger et al. (2025a) showed that hydrated aerosols still have a substantial impact on fog microphysical properties in the region. Against this background, and based on sensitivity experiments using the LES, we aim to address the following questions:

1) What meteorological and microphysical conditions are critical for capturing the general characteristics of the observed fog properties and life cycle?

2) How sensitive are the fog properties to aerosol physics, including the total particle number concentration, particle mean size, and modal width?

3) What is the role of aerosol chemistry for the fog properties under different pollution conditions, and what is the importance of hydrated aerosols?

4) How important is the model representation of the droplet size distribution, and how do variations in droplet microphysical parameters affect the fog behavior?

2 Data and methods

2.1 Case description

The FAIRARI campaign 2021/22 (Neuberger et al., 2025b) was conducted at the San Pietro Capofiume site (SPC, 44.65°N, 11.62°E) in Italy, which represents a background-polluted continental environment in the eastern Po Valley. We focus on three
90 consecutive radiation fog events that took place during the winter of 2022, labeled as events 7, 8, and 9 (Neuberger et al., 2025b) (see Fig. 1a). The series of events began at 18:49 LST (local standard time, UTC+1) on 18 February, and the fog dissipated completely by 07:38 LST on 19 February, with a mean visibility ranging between 66 and 151 m. The fog formation was triggered by longwave radiation loss and nocturnal surface cooling, leading to air saturation and aerosol activation. The near-surface layer was stably stratified, characterized by weak turbulence (mean turbulent kinetic energy, TKE $\sim 0.011\,\mathrm{m^2 s^{-2}}$)
95 and light winds (mean speed $\sim 0.6\text{-}0.9\,\mathrm{m\,s^{-1}}$), predominantly from the southeast to the south (125°-200°). The stable conditions favored the accumulation of a high aerosol load (mean number concentration for particles with diameters 13.3-792 nm, N_a $\sim 6065\,\mathrm{cm^{-3}}$) and fog droplets (mean number concentration for droplets with diameters 2-60 μm, $N_c \sim 59\,\mathrm{cm^{-3}}$ and effective diameter, ED $\sim 13\,\mathrm{\mu m}$) close to the surface and a progressively increasing optical thickness of the fog layer during the evening and early night.
100 The aerosol chemical composition in terms of mass was dominated by ammonium nitrate, ammonium sulfate, and organics, with minor fractions of chloride and black carbon (Fig. 2), and can be described with a median hygroscopicity parameter κ of approximately 0.45 during the fog events, indicating rather hygroscopic aerosols. The high κ promoted hygroscopic aerosol growth and the formation of haze particles (i.e., hydrated particles), which substantially influenced the fog microphysics, particularly droplet number concentration and effective diameter (see further discussion in Neuberger et al., 2025a). As a result
105 of their hygroscopic growth, hydrated particles also contribute to a bimodal droplet size distribution (Fig. 1a and Fig. 3a). In this study, hydrated and activated particles were simply separated according to this bimodal distribution: particles associated with the first peak (below approximately 10 μm, see Fig. 1a) were considered hydrated particles, while those larger than 10 μm were categorized as activated droplets. During the three fog events, two brief interruptions were observed (at 00:14-01:14 LST and 04:02-04:14 LST), characterized by a temporary disappearance of large droplets and a sharp decrease in LWC, leaving
110 only residual haze particles (Fig. 1a). We suggest that these interruptions were caused by short-term near-surface warming that led to droplet evaporation, although the precise local meteorological drivers remain unclear (see Sect. 3.1).
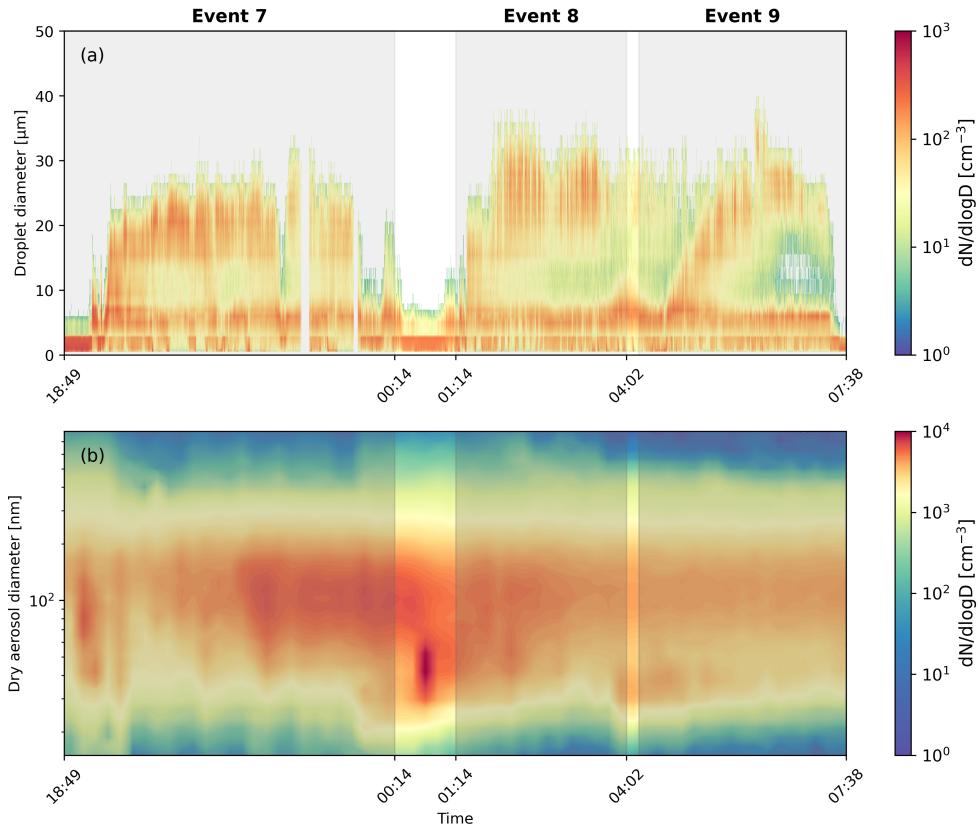
Figure 1. Observed near-surface (a) droplet spectrum and (b) dry aerosol spectrum for fog events 7, 8, and 9 on 18–19 February 2022. The shaded gray areas indicate periods with fog (see also Neuberger et al., 2025b).

2.2 Model description

The simulations were carried out using the MISU–MIT Cloud and Aerosol model (MIMICA; Savre et al. 2014), a three-dimensional LES code that solves the equations describing a non-hydrostatic, incompressible atmospheric system. The model

115 employs a 1.5-order subgrid-scale turbulence closure scheme and computes surface fluxes using Monin–Obukhov similarity theory (Stull, 1988), enabling the representation of the exchange of momentum, heat, and moisture between the surface and atmosphere under specified surface forcing. Warm cloud microphysics is represented using a two-moment bulk scheme (Seifert and Beheng, 2001, 2006), which predicts the mass mixing ratios and number concentrations of hydrometeors. The mass distributions of cloud droplets and raindrops are described by gamma functions. Raindrop terminal velocities follow a power-law

120 relationship (Seifert and Beheng, 2006; Savre et al., 2014), while cloud droplet terminal velocity is computed based on a generalized gamma distribution within the Stokes regime and is incorporated into the prognostic equations for droplet number concentration N_c and liquid mixing ratio Q_c (see Sect. S1). Supersaturation is explicitly resolved using the pseudo-analytical approach of Morrison and Grabowski (2008), with its effects on condensation and evaporation integrated at each time step.

MIMICA includes an interactive aerosol scheme, where aerosols are described using a two-moment module with all aerosol modes following lognormal size distributions (Ekman et al., 2006). The aerosol number size distribution with respect to particle radius r in mode k is given by:

$$\frac{\mathrm{d}N_{a,k}}{\mathrm{d}r} = \frac{N_{a,k}}{\sqrt{2\pi}\, r \ln \sigma_k} \exp\left[-\frac{(\ln r - \ln r_{g,k})^2}{2\ln^2 \sigma_k}\right], \tag{1}$$

where $N_{a,k}$ is total aerosol number concentration, $r_{g,k}$ is geometric mean radius and σ_k is geometric standard deviation for mode k.

In the present study, the aerosol size distribution is represented by one mode, covering the measured size range of 13.3-792 nm. Aerosol hygroscopic growth and activation into droplets are calculated based on κ-Köhler theory (see Sect. S2). Consistent with the lower measurement threshold common in fog monitors (Neuberger et al., 2025a), particles with wet diameters larger than 2 μm are typically classified as fog droplets. To further investigate the role of fog droplets with different sizes in fog processes, a more detailed classification is applied here: particles that have grown a wet diameter above 2 μm but do not reach the activation size are categorized as hydrated aerosols, whereas those exceeding the activation size (determined by κ-Köhler theory) are counted as activated droplets. Accordingly, the number concentration of total droplets N_c is the sum of hydrated aerosols $N_{c,\mathrm{hyd}}$ and activated droplets $N_{c,\mathrm{act}}$:

$$N_c = N_{c,\mathrm{hyd}} + N_{c,\mathrm{act}} = \int\limits_{D_{\min=2\mu\mathrm{m}}}^{D_{\mathrm{act}}} n(D)\,dD + \int\limits_{D_{\mathrm{act}}}^{\infty} n(D)\,dD. \tag{2}$$

Radiative transfer is computed using a four-stream scheme (Liou, 1993), which includes six bands for solar radiation and twelve bands for the infrared part. This scheme accounts for the radiative effects of cloud droplets and raindrops, allowing a dynamic coupling between radiation and cloud microphysical processes. Note that the aerosol particles do not directly affect the radiative transfer, only indirectly by altering the fog microphysical properties.

Based on the above schemes, the diagnosed microphysical quantities of total droplets are used to characterize the fog life cycle and optical properties. Fog periods are defined by a Vis ≤ 1 km and RH $\geq 90\%$ (Neuberger et al., 2025b), where the parameterized visibility Vis is calculated as a function negatively correlated with LWC and N_c (Gultepe et al., 2006):

$$\mathrm{Vis} = \frac{1.002}{(\mathrm{LWC} \cdot N_c)^{0.6473}} = \frac{1.002}{(\rho_{air} Q_c \cdot N_c)^{0.6473}}, \tag{3}$$

where ρ_{air} is the air density and Q_c is liquid mixing ratio. This parameterization is applicable for LWC in the range of 0.005-0.5 g m⁻³ and N_c within 1-400 cm⁻³.

The liquid water path LWP and optical thickness τ of the fog layer are calculated following Morrison and Grabowski (2007)

150 and Brenguier et al. (2011) as:

$$\text{LWP} = \int\limits_{\text{fog}_{\text{base}}}^{\text{fog}_{\text{top}}} \text{LWC}(z)\,dz = \int\limits_{\text{fog}_{\text{base}}}^{\text{fog}_{\text{top}}} \rho_{\text{air}}(z)\,Q_c(z)\,dz, \tag{4}$$

$$\tau = \frac{3\,\text{LWP}}{2\,\rho_w\,r_{\text{eff}}}, \tag{5}$$

where the fog top and base heights are determined from grid cells meeting the criteria: $N_{c,\text{act}} \geq 1$ cm^{-3} and $Q_c \geq 0.01$ g kg^{-1}

155 (Maronga and Bosveld, 2017); ρ_w is the density of liquid water, ρ_{air} the air density, and the droplet effective radius is calculated

as $r_{\text{eff}} = \left(\frac{3\,Q_c\,\rho_{\text{air}}}{4\pi\,\rho_w\,N_c} \right)^{1/3}$.

2.3 Simulation setup

Our reference simulation was initialized at 18:00 LST on 18 February 2022 and continued until 14:00 LST the following

day, with a temporal resolution of approximately 1.0 second. Simulation tests showed that this time step optimally balanced

160 numerical accuracy in resolving the supersaturation evolution and computational efficiency. A coarser time step was found to

overestimate local supersaturation and droplet activation (Schwarz et al., 2024). The simulation domain was 0.16 km × 0.16 km

× 1.6 km, with a grid spacing of 5 m × 5 m × 2 m.

The initial vertical profiles of temperature and humidity were configured using a combination of radiosonde observations at

SPC and ECMWF Reanalysis (ERA5, Hersbach et al., 2023). The radio sounding and reanalysis both indicated warm-air

165 advection above the fog layer around 22:00 LST. To reproduce this feature, we applied nudging based on the ERA5 profiles

between 21:30 and 22:30 LST (Fig. S1 in the Supplementary Information). The initial horizontal wind field was set to zero,

in agreement with observations and reanalysis that showed weak near-surface winds and wind shear. Since the series of fog

events was mainly driven by radiative cooling with negligible vertical motion, the initial updraft was also set to zero. For the

surface forcing, the surface skin temperature SST was prescribed using 3.5-m temperature observations starting from 18:00

170 LST (Fig. S2). Due to the absence of soil moisture observations, the baseline surface skin moisture SSM was also interpolated

based on the 3.5-m data, which were saturated during nighttime. At sunrise, the 3.5-m humidity measurements remained

saturated and were thus not representative of the response of soil moisture to shortwave heating. To account for surface heating

and subsequent evaporation, we estimated the surface relative humidity RH (in %) after sunrise using the revised Tetens formula

(Alduchov and Eskridge, 1996):

175 $$\text{RH} = \frac{e}{e_s(T)} \cdot 100 = \exp\left(\frac{17.625\,T_d}{T_d + 243.04} - \frac{17.625\,T}{T + 243.04} \right) \cdot 100, \tag{6}$$

where the dew point temperature (T_d) was approximated by the nocturnal minimum temperature. The influence of surface forcing is further discussed in Sect. 3.1 and Sect. S5, where sensitivity tests are labeled as SFC_SST and SFC_SSM.

The observed aerosol size distribution showed a relatively large variability during the series of fog events (see Fig. 1b), with total number concentrations ranging between 4,067 and 9,927 cm^{-3}. Given the very low aerosol activation rate (<1%, cf. Neuberger et al., 2025b), aerosol scavenging and regeneration processes were neglected, and the dry aerosol population was kept close to the fitted observational means during the simulations. In the lognormal distribution fitting, priority was placed on ensuring that the particle size distribution and spectral mean diameter of the accumulation mode matched the observed spectrum, as large particles in these size ranges dominated activation, as suggested by Neuberger et al. (2025a). Specifically, the total aerosol concentration was set to 5,000 cm^{-3}, the mean radius to 48.2 nm, and the standard deviation to 1.9. The chemical composition of the aerosol mixture was prescribed as constant, based on the observational mean, represented by a molar weight of 49.35 g mol^{-1}, a density of 1,618.62 kg m^{-3}, and an average κ of 0.45, with its individual chemical components shown in Fig. 2. As mentioned in Sect. 2.2, the prescribed shape of the droplet size distribution in MIMICA follows a gamma distribution. Fig. 3a shows the observed fog droplet size distribution, together with different idealized gamma distributions using a range of shape parameters. As discussed in Neuberger et al. (2025b), the observations show a clear bimodal droplet size distribution, with one peak around 6 μm, associated with non-activated hydrated particles, and a second peak around 10-40 μm, associated with activated fog droplets. For the reference simulation, we used a distribution with shape parameters $\alpha = 3$ and $\nu = 1$, which reasonably captures the observed mean activated droplet spectrum (Fig. 3). The peak associated with the hydrated aerosols is predicted in MIMICA by the aerosol module using κ-Köhler theory (see Sect. S2).

Additionally, given the small average droplet size and the correspondingly low collision efficiency and following the recommendation from Riipinen et al. (2025), the collision-coalescence process was turned off in MIMICA in the reference simulation (tests with collision-coalescence enabled are presented in Sect. S4). The droplet autoconversion term was also excluded due to the absence of precipitation in the observations. Notably, by deactivating these two processes, the droplet size distribution in the model can be maintained largely consistent with that implied by the prescribed shape parameters; otherwise, potential adjustments to the droplet size distribution through collision–coalescence and autoconversion could introduce inconsistencies with the droplet spectrum corresponding to sedimentation rates calculated based on the prescribed shape parameters.
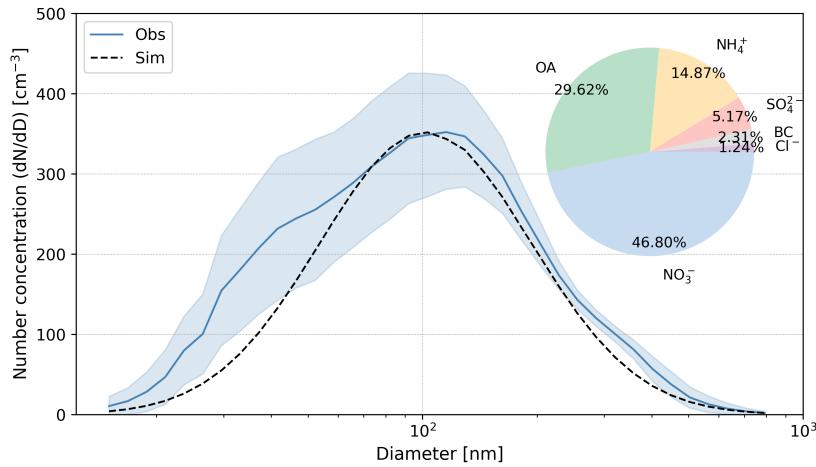
Figure 2. Initial aerosol number size distribution and chemical composition mass fractions used in the reference simulation (Sim), fitted from the observed mean aerosol spectrum over the fog events (Obs), with the shaded area indicating ±1 standard deviation.

2.4 Sensitivity experiments

To address the research questions outlined in the introduction and, specifically, to quantify the responses of fog properties to variations in aerosol regimes and droplet microphysical representations, we conducted sensitivity experiments. To systematically evaluate the effects of individual parameters while minimizing parameter interactions, we implemented the one-at-a-time (OAT) sensitivity for the tests. An overview of the experimental design is given in Table. 1.

2.4.1 Aerosol physics

The aerosol size distribution critically determines both the number of CCN and their activation efficiency (Dusek et al., 2006; Rose et al., 2010). Here, we focus our analysis on changes in the total aerosol number concentration (N_a). Similar to non-surface clouds, for a constant LWC, an increase in N_a generally produces a higher concentration of smaller droplets, which enhances the cloud's optical thickness and impacts the radiative properties (Twomey, 1977). Furthermore, smaller droplet sizes also suppress autoconversion and the formation of precipitation, which reduces sedimentation rates and can lead to an extended residence time of liquid water (Albrecht, 1989; Yan et al., 2021), i.e. a longer fog duration (Stolaki et al., 2015; Maalick et al., 2016; Yan et al., 2020). For this study, N_a was varied from 2,000 to 24,000 cm^{-3} with 2,000 cm^{-3} intervals (labeled as AERO_NA*). The chosen range of aerosol concentrations was based on observations from the Po Valley during the 1980s–1990s as well as the recent FAIRARI campaign (Noone et al., 1992; Neuberger et al., 2025b).

In the sub-micron size range, nucleation mode and Aitken mode particles typically originate from local emissions, whereas accumulation mode aerosols often undergo coagulation and long-range transport, and generally exhibit higher activation efficiency (Seinfeld and Pandis, 2016). For a log-normal aerosol size distribution, variations in modal composition are reflected in predefined geometric mean radius r_g and standard deviation σ: smaller r_g and σ values are usually associated with locally

sourced, single-origin particles, whereas larger r_g and σ indicate a greater contribution from accumulation mode particles that have aged, are internally mixed, and exhibit multi-source characteristics.

To investigate the response of fog to changes in the aerosol spectral parameters, sensitivity experiments were conducted by perturbing σ and r_g by $\pm 5\%$ and $\pm 10\%$ within the observed range of variation for the fog events (denoted as AERO_SIG* and AERO_RG*, respectively). Positive perturbations shift the size distribution toward the accumulation mode, while negative perturbations enhance the relative contribution of nucleation and Aitken mode particles. The perturbed size distributions were compared with the observed spectrum, showing that the mean relative deviation (MRD, defined as the average of the relative errors across sizes normalized by the observational standard deviation) does not exceed 1.5 SD for negative perturbations while remaining below 0.7 SD for positive perturbations. The responses of fog properties to these perturbations are presented in Sect. S6.

2.4.2 Aerosol chemistry

Building upon the discussion in Sect. 1 regarding the role of aerosol chemical composition under different pollution conditions, we developed a series of κ perturbation experiments ($\pm 10\%$, within the range observed during fog events 7-9) across varying aerosol loading to further quantify the impact. For typical clean conditions ($N_a < 2,000 \, \text{cm}^{-3}$), which are rarely observed in the Po Valley, the background aerosol composition was initialized using observations from the Hyytiälä site (Heikkinen et al., 2020), with a baseline bulk κ of 0.27, and N_a set to 200, 600, 1,000, and 2,000 cm^{-3}. For the polluted scenarios, the baseline aerosol composition and κ (0.45) were the same as in the reference simulation, while N_a was set to 6,000, 12,000, 18,000 and 24,000 cm^{-3}. The simulations under clean and polluted conditions are labeled as AERO_NA*KC* and AERO_NA*KP*, respectively. Note that σ and r_g were kept the same in all simulations here.

2.4.3 Droplet microphysics

To investigate the sensitivity of fog development to variations in the prescribed droplet size distribution, the observed mean droplet spectrum was fitted with a general gamma distribution. Based on the fitting results, as well as typical distributions reported in previous studies (e.g., Contreras Osorio et al., 2022), a series of α and ν shape parameter combinations (Fig. 3, labeled as DROP_A*N*, where A stands for α and N for ν) were selected and systematically evaluated. The results indicate that medium width spectrum combinations [2,3] and [2,4], as well as [3,1], which was used in the reference simulation, provide a good fit for the activated droplet range (diameter > 10 μm) (Fig. 3b). The potential impact of wider spectrum combinations, which may be less physically realistic but have been adopted in previous studies (e.g., Contreras Osorio et al., 2022), was also examined.
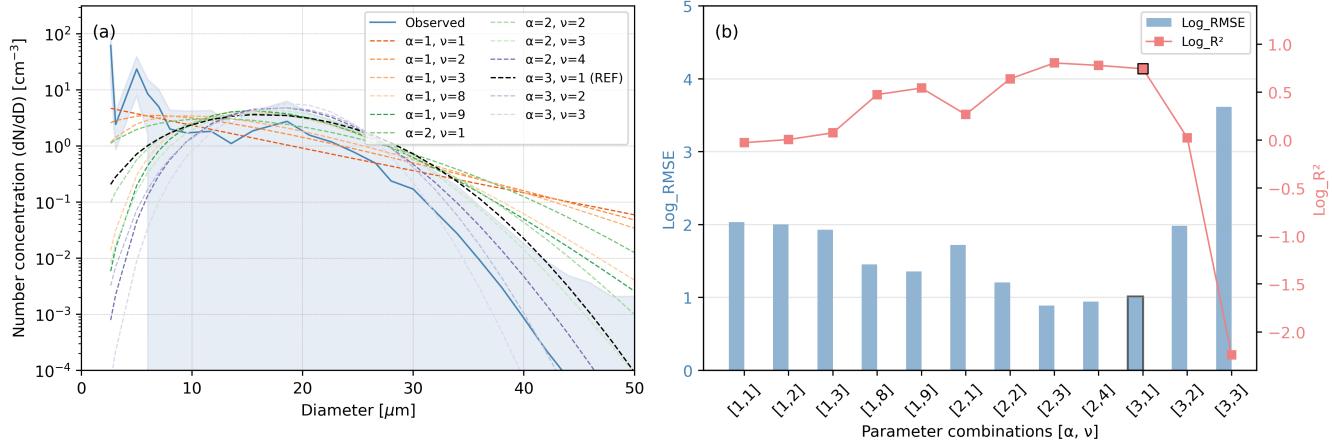
Figure 3. (a) Comparison of observed mean droplet number size distribution (solid line) and model-fitted generalized gamma distributions (dashed lines) for different combinations of shape parameters α and ν. The shaded area represents ± 1 standard deviation. (b) Goodness-of-fit in log-space for the corresponding parameter combinations in the activated particle range (> 10 µm), with blue bars representing the root mean square error (RMSE) and red lines representing the coefficient of determination (R^2).

Table 1. Summary of sensitivity experiments. Key parameters include SST (surface skin temperature) and SSM (surface skin moisture) for surface forcing; N_a (aerosol number concentration), r_g (geometric mean radius) and σ (geometric standard deviation) for aerosol log-normal distribution; and α, ν (shape parameters) for droplet gamma distribution.

Experiment category	Simulation label	SST	SSM	N_a (cm^{-3})	r_g (nm)	σ	κ	$[\alpha, \nu]$
Reference simulation	REF	ref	ref	5,000	48.2	1.9	0.45	[3, 1]
Surface forcing	SFC_SST*	*-0.5K, -1.0K, -2.0K, -3.0K	–	–	–	–	–	–
	SFC_SSM*	–	*VAR, 0.95, 0.90, 0.85	–	–	–	–	–
Aerosol physics	AERO_NA*	–	–	*2,000–24,000	–	–	–	–
	AERO_RG*	–	–	–	*$r_g \pm 5\%$, $r_g \pm 10\%$	–	–	–
	AERO_SIG*	–	–	–	–	*$\sigma \pm 5\%$, $\sigma \pm 10\%$	–	–
Aerosol chemistry (Clean conditions)	AERO_NA*KC*	–	–	*200, 600, 1000, 2000	–	–	κ_c, $\kappa_c \pm 10\%$	–
Aerosol chemistry (Polluted conditions)	AERO_NA*KP*	–	–	*6,000, 12,000, 18,000, 24,000	–	–	κ_p, $\kappa_p \pm 10\%$	–
Droplet microphysics	DROP_A*N*	–	–	–	–	–	–	*[1,1],[1,2],[1,3],[1,8], [1,9],[2,1],[2,2],[2,3], [2,4],[3,2],[3,3]

3 Results and discussion

3.1 Reference simulation

250 The reference simulation (REF, Fig. 4) serves as a baseline for our study and is compared to observational data (Fig. 5 and Fig. 6) to evaluate the model performance. Fig. 4 shows the time height evolution of in-fog properties. Nocturnal longwave

radiative cooling at the surface results in supersaturated air, droplet activation, and fog formation around 19:30 LST. The fog top lifting is mainly attributed to sustained radiative emission by the droplets, with additional contributions from air radiative loss and turbulent diffusion (Price, 2011; Dimitrelos et al., 2020). For the present case, the presence of advected warm air above the fog limits the vertical development. Neglecting the advection, and thus the entrainment of warm, dry air at the fog top, results in a considerably thicker fog layer and an extended fog lifetime compared to the REF simulation (see Sect. S4). As the fog develops and becomes optically thick, the region of strong radiative cooling shifts gradually from the surface to the fog top, where supersaturation and droplet concentrations reach peak levels. During the mature stage (e.g., 00:00-02:00 LST), the negative buoyancy generated by fog-top cooling, together with a weak surface warming (Fig. S2), renders the fog layer thermodynamically unstable and triggers convection. This enhances the mixing within the fog layer and suppresses droplet sedimentation, resulting in relatively high droplet number concentrations and liquid water content. After sunrise, near-surface warming induces droplet evaporation, leading to a decoupling of the fog layer from the surface. In addition, droplet sedimentation is found to play an important role in fog dissipation. If the sedimentation scheme is disabled (see Sect. S4), fog liquid water content, droplet number and geometrical thickness are significantly overestimated, and the dissipation is also delayed compared to observations.

The near-surface microphysics and visibility time series are evaluated against the observations in Fig. 5. MIMICA simulates the dissipation phase well, but the onset occurs approximately 41 minutes later than observed. This delay is likely related to uncertainties in the prescribed surface forcing, as the REF simulation relies on 3.5-m air temperature due to the absence of in-situ ground surface temperature measurements. In stable boundary layers, the ground surface is typically colder than the near-surface air and cools at a faster rate, as also reported in early Po Valley field campaigns (Wobrock et al., 1992). Sensitivity experiments with surface temperature perturbations of $-0.5\,\mathrm{K}$ to $-3.0\,\mathrm{K}$ confirm that lowering the surface temperature results in earlier fog onset (see Fig. S4a), consistent with Price (2011), who noted that locally cooler or moister surfaces tend to favor fog formation.

The simulated near-surface supersaturation (0.0034%-0.0294%, mean 0.0129%) is in reasonable agreement with observational supersaturation constraints (0.0117%-0.0238%, mean 0.0165%; Neuberger et al. 2025a), indicating that the REF simulation realistically captures the local microphysical conditions governing droplet activation. The model also reproduces the observed mean droplet size reasonably well but overestimates the number of activated droplets and the liquid water content (Fig. 5c, a, and b, respectively), which is a common issue when using bulk microphysics schemes (Schwenkel and Maronga, 2019; Boutle et al., 2022). This overestimation is particularly pronounced for large droplets. As shown in Fig. 6, the simulated number concentration of droplets larger than $25\,\mu\mathrm{m}$ is substantially higher than observed, except for event 8. These large droplets dominate the total fog water and are most likely the primary reason for the positive modeled bias in liquid water mixing ratio (Fig. 5). However, the surface flux of water vapor also plays a crucial role in regulating the liquid water content. A series of sensitivity experiments was conducted, where the surface relative humidity was set to 85%, 90%, and 95% (SSM_085, SSM_090, and SSM_095) and the nocturnal surface warming and evaporation processes based on Eq. (6) were refined (labeled as SSM_VAR). These adjustments effectively reduce droplet numbers and liquid water relative to REF, and in some cases

(e.g., SSM_090 and SSM_085), the model has the potential to capture water loss and non-fog periods between fog events (see Sect. S5).
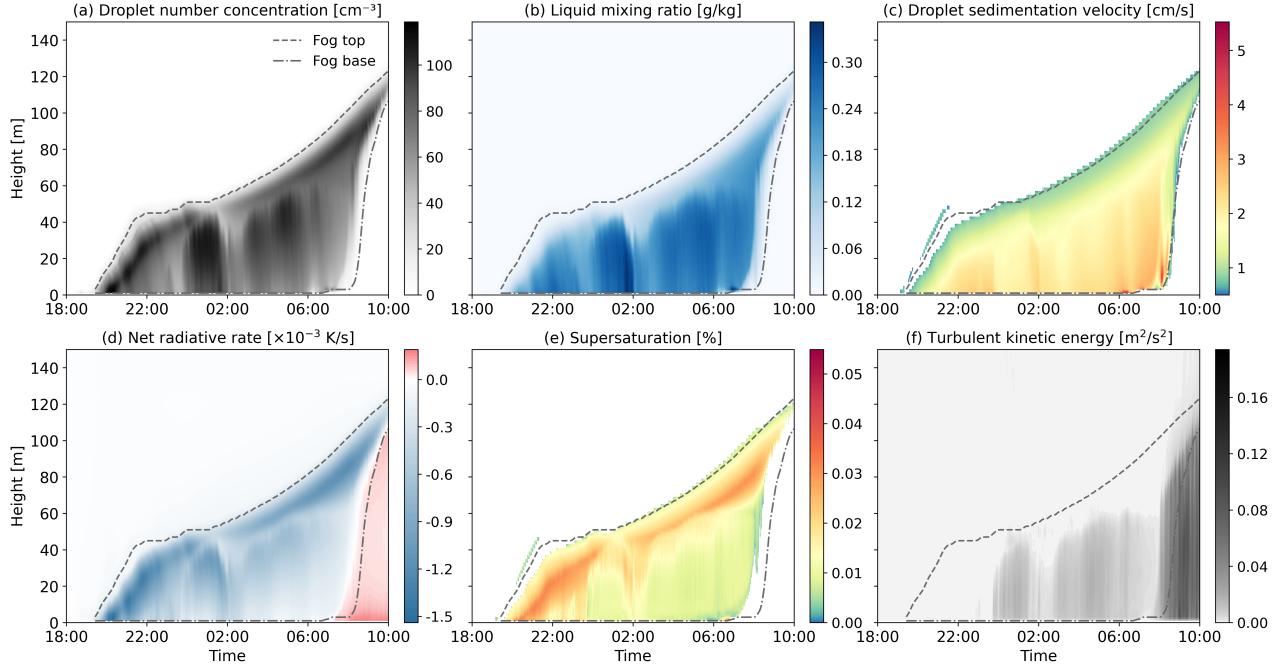
Figure 4. Time–height cross-sections of horizontally averaged fog properties in the reference simulation: (a) droplet number concentration, (b) liquid water mixing ratio, (c) droplet sedimentation velocity, (d) net radiative temperature rate, (e) supersaturation and (f) turbulent kinetic energy. The fog top and base are shown as dashed and dash-dotted gray lines.
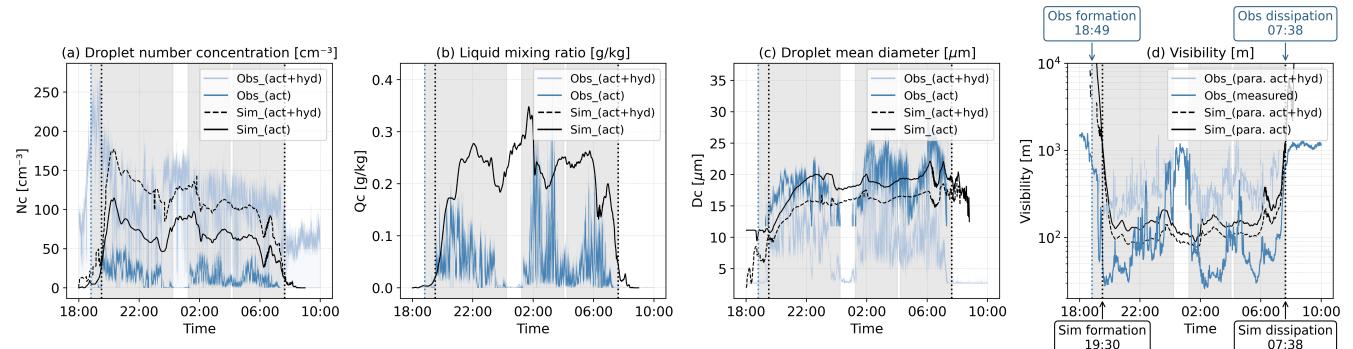
Figure 5. Time series of near-surface (a) droplet number concentration, (b) liquid water mixing ratio, (c) droplet mean diameter and (d) measured and parameterized (para.) visibility from observations (obs) and simulations (sim) for the whole fog event, where "act" refers to activated droplets only and "act+hyd" includes both activated droplets and hydrated aerosols. The shaded gray areas indicate fog periods identified from the observation. Note that this figure differs slightly from Fig. 11 in Neuberger et al. (2025a) due to updated meteorological conditions and fog period criteria in the current study.

In contrast to the overestimation of activated droplets, MIMICA reproduces fewer hydrated particles than observed (Fig. 5), which is most likely because the hygroscopic growth factor in the model is calculated using a bulk-averaged method, that is,

290 all dry particles take up water vapor with the same factor (see Sect. S2). In reality, due to the Kelvin effect, small particles have a high surface curvature, which increases their equilibrium vapor pressure and inhibits water uptake, whereas larger particles have lower curvature and can absorb water more easily. In other words, the hygroscopic growth factor should increase with particle size, meaning that larger particles should grow more than smaller ones (see the comparison between observed and simulated wet aerosols in Fig. 6). Note that when comparing the total number of droplets (i.e., hydrated particles + activated

295 droplets), the model agrees well with observations, indicating that the high bias in activated droplets is partially compensated by the low bias of hydrated particles. Due to their small size, simulated hydrated particles do not contribute substantially to the total fog water content (<1%). Consequently, and in line with Boutle et al. (2018), our simulations show that the development of a well-mixed fog layer is primarily driven by the activated droplets; deactivating the hygroscopic growth scheme in MIMICA has a negligible effect on fog thickness τ and liquid water path LWP (see Sect. S4). However, in visibility parameterizations,

300 neglecting the hydrated particles may result in an overprediction of visibility (17.80%-79.03%, mean 39.64%) and biases in fog period estimation (Fig. 5d).
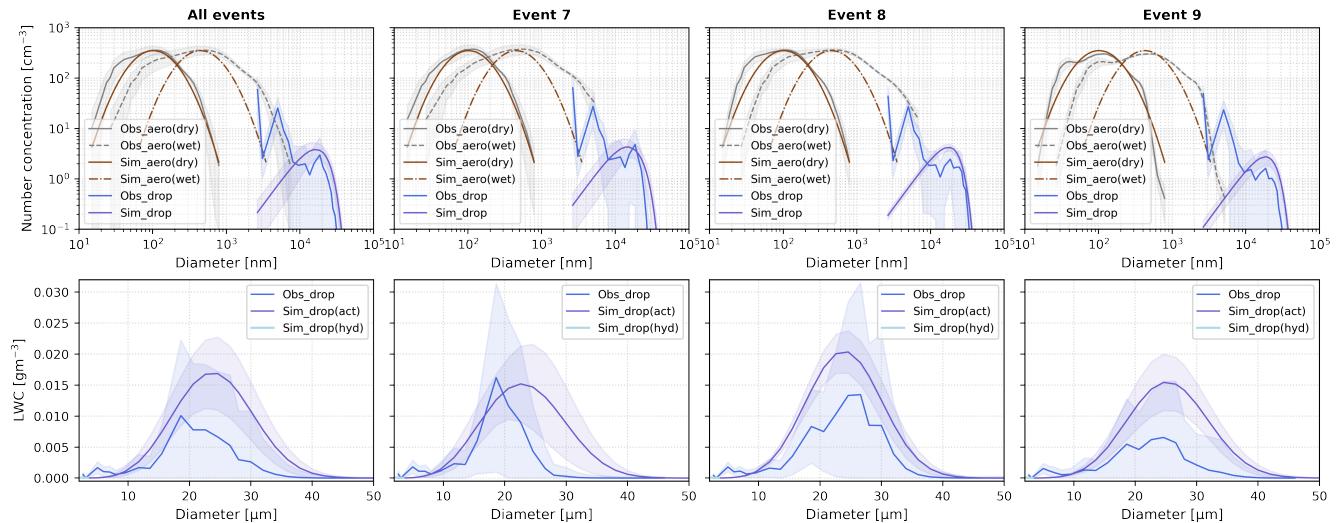
Figure 6. Size distributions of observed (Obs) and simulated (Sim) aerosols and fog droplets, averaged over fog events 7, 8, and 9. Upper panel: number concentrations, lower panel: LWC. "Dry" and "wet" refer to aerosols before and after hygroscopic growth, respectively. Shaded areas indicate ±1 standard deviation. Note that the LWC of simulated hydrated droplets (Sim_drop (hyd)) is visible only within a very narrow diameter range in the lower left corner of the LWC panel.

3.2 Sensitivity to aerosol physics

As described in Sect. 2.4.1, to assess the impact of aerosol number concentration N_a on fog properties, we conducted the AERO_NA sensitivity experiments, with N_a varying from 2,000 to 24,000 cm^{-3} in 2,000 cm^{-3} increments. With higher N_a, the

305 number of both activated and hydrated particles increases, resulting in a higher liquid water content and a decrease in visibility

(Fig. 7c,d,h). At the same time, the longwave radiative cooling is enhanced, which increases negative buoyancy and elevates TKE, thereby promoting stronger fog layer mixing during the mature stage. Under conditions of nearly constant water vapor available for condensation, stronger competition for vapor reduces the mean droplet radius (Fig. 7e), which is consistent with the Twomey effect in clouds (Twomey, 1977), and was also observed during the field campaign (Neuberger et al., 2025a).

310 In addition, enhanced competition suppresses ambient supersaturation, resulting in a smaller fraction of particles that can be activated (i.e., the activation fraction in Fig. 8a). The droplet conversion fraction, i.e., the ratio of the total droplet number to the aerosol number, also decreases with increasing N_a; nevertheless, the relative contribution of hydrated particles to the total droplet population increases and becomes dominant at around $N_a = 12{,}000\,\mathrm{cm}^{-3}$ (Fig. 8b). In other words, variations in total N_c are largely attributable to changes in the number of hydrated particles at high aerosol concentrations. Considering

315 the underestimate of the hygroscopic growth factor noted in section 3.1, their actual contribution should be higher, and the threshold N_a where they start to dominate the total droplet number concentration is likely lower.

For cases with $N_a < 14{,}000\,\mathrm{cm}^{-3}$ (excluding $N_a = 8{,}000\,\mathrm{cm}^{-3}$), the fog lifetime is prolonged with increasing N_a, manifested as slightly earlier formation and a more pronounced, delayed dissipation (Fig. 7a,b). The earlier onset is due to the reduction in visibility caused by the numerous hydrated particles under high N_a conditions during the initial stage of the fog, when

320 droplet activation has not become dominant yet. The delayed dissipation can, in our simulations, be attributed to the reduced sedimentation rates that extend the residence time of fog droplets (Fig. 7g), consistent with the cloud lifetime effect (Albrecht, 1989). The amount of shortwave radiation that reaches the surface is also reduced, which, in reality, should dampen surface warming and slow down droplet evaporation (Jia et al., 2019; Yan et al., 2020). However, in our simulations, the surface forcing was kept identical across all N_a cases. Consequently, the suppression of near-surface droplet evaporation under high

325 N_a is likely underestimated.

Moreover, the response of fog lifetime to N_a is nonlinear; for $N_a > 12{,}000\,\mathrm{cm}^{-3}$, fog duration becomes almost insensitive to further increases in N_a. This result shows that differences in sedimentation rates and the resulting impact on visibility become negligible under extremely high pollution conditions (Fig. 7g,h). Fig. 8c also shows that the relative sensitivity of N_c to changes in N_a declines sharply at high N_a, primarily due to the availability of water vapor and supersaturation.

330 Fig. 9 shows the fog height and optical properties for the AERO_NA experiments. In contrast to Stolaki et al. (2015), where halving or doubling the CCN concentration was found to alter fog height by around 35%, our results show a small influence of changing N_a. When N_a is doubled, the fog-top height increases on average by no more than 4%. Even across all AERO_NA cases, the average fog top increase does not exceed 11%. This suggests that the vertical structure of the fog layer is governed primarily by radiative cooling and turbulent mixing rather than any aerosol effects. By comparison, N_a exerts a more pro-

335 nounced effect on the LWP and fog optical thickness, where the elevated N_c and LWC with increasing N_a are a result of not only more activation but also reduced sedimentation that prolongs the droplet residence time.
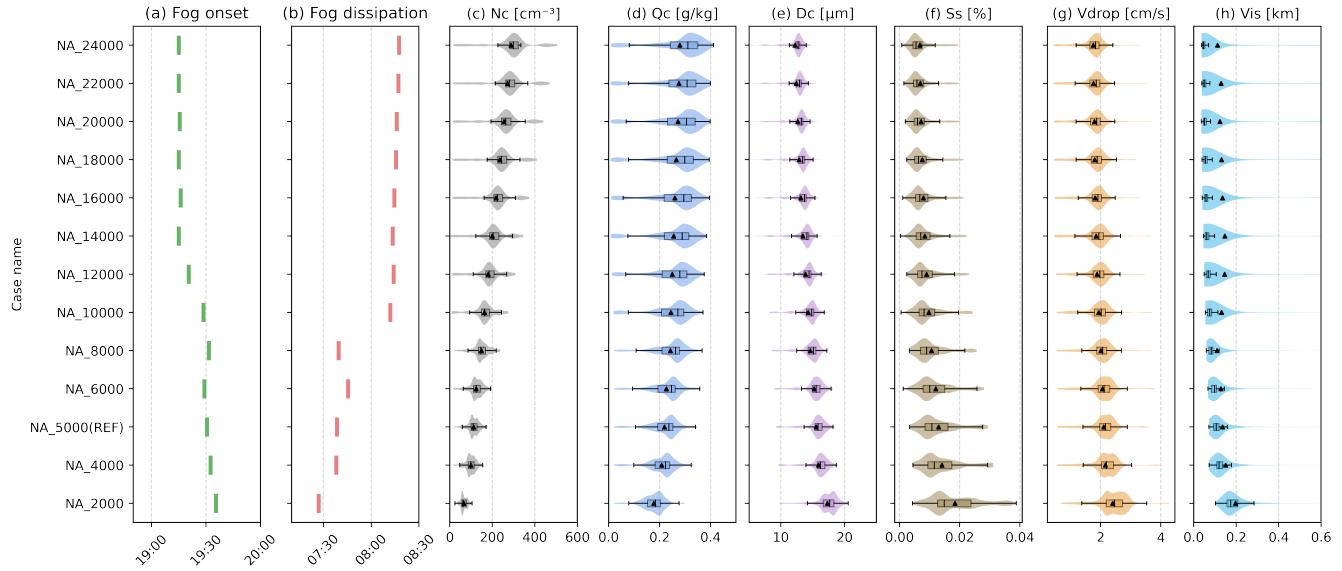
Figure 7. Statistical near-surface fog properties in AERO_NA experiments: (a) fog onset time, (b) fog dissipation time, (c) total droplet number concentration N_c, (d) liquid water mixing ratio Q_c, (e) mean droplet diameter D_c, (f) supersaturation Ss, (g) droplet sedimentation velocity V_{drop} and (h) visibility Vis. The visibility is dependent on both activated and hydrated particles, see Sect. 2.2. The boxes represent the 25th-75th percentiles, whiskers the 5th-95th percentiles, the solid line the median, and the black triangle the mean. Shaded areas illustrate the distribution of values.
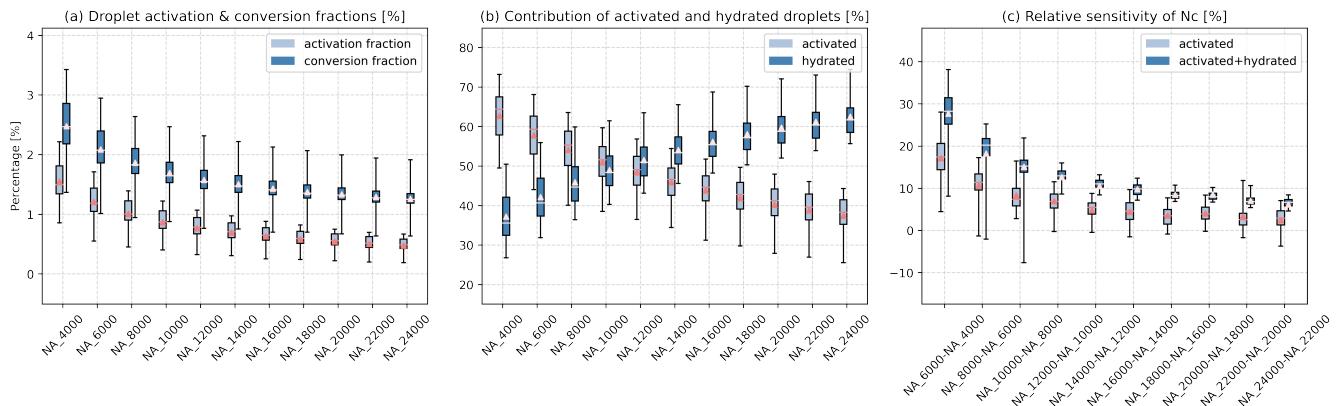
Figure 8. N_c-related statistical results in the AERO_NA experiments: (a) droplet activation and conversion fraction, where the activation fraction = $N_{c,act}/N_a \times 100\%$, and the conversion fraction = $(N_{c,act} + N_{c,hyd})/N_a \times 100\%$, (b) contribution of activated and hydrated particles to total droplet population, and (c) relative sensitivity of N_c with increased N_a, which is quantified as the percentage change in N_c relative to the lower-N_a scenario between two consecutive N_a cases differing by 2000 cm-3 over their overlapping fog period. The light blue boxes represent activated particles, and dark blue ones include hydrated particles.
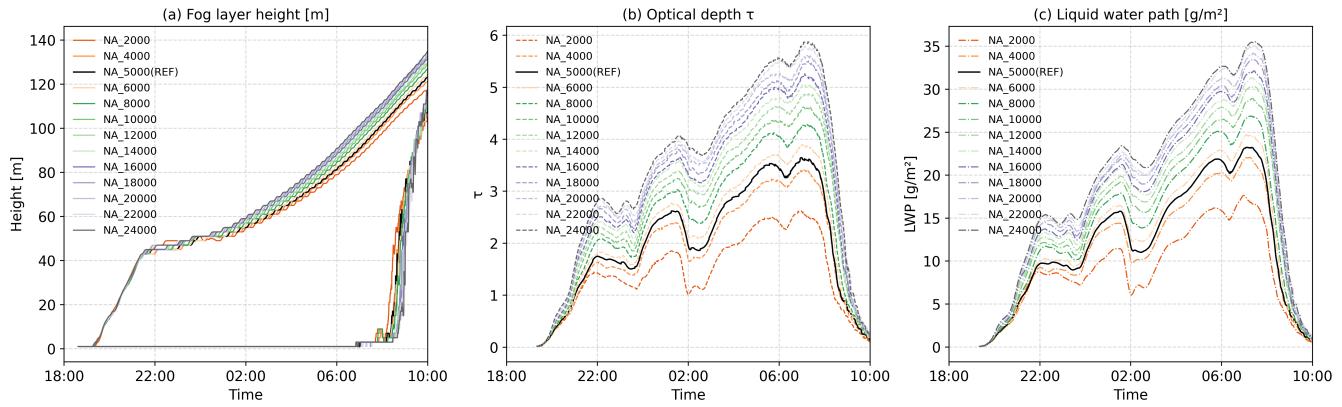
Figure 9. Vertical fog properties in AERO_NA experiments: (a) fog layer height, (b) optical thickness and (c) liquid water path.

3.3 Sensitivity to aerosol chemistry

The response of fog to aerosol chemistry was examined through κ perturbation experiments under different pollution scenarios (see Sect. 2.4.2). With a higher κ, the number concentration of activated droplets (Fig. 10a and c) increases, which in turn

340 leads to a decrease in the visibility (Fig. 10b and d) and an increase in the LWP and optical thickness (not shown) compared to the baseline case. This can be explained by the decrease in the dry activation diameter. However, the sensitivity to κ varies under different pollution scenarios. Overall, the number of activated droplets is more sensitive to κ perturbations under clean conditions, i.e. with lower N_a and κ (Fig. 10a); Except for $N_a = 200\,\text{cm}^{-3}$, the relative changes in $N_{c,act}$ range from +6.6% to +7.8% when κ is increased by 10% and from –7.3% to –5.9% when κ is reduced by 10%, which is generally higher than the

345 corresponding changes for polluted conditions (+4.0% to +5.5% and –5.5% to –4.2%, respectively, Fig. 10a). The visibility calculated using only activated droplets ($N_{c,act}$) in Eq. (3) shows a similar result (Fig. 10b). However, when hydrated particles are considered, the sensitivity of the total number concentration of droplets to κ perturbations exhibits a different pattern, with greater sensitivity under polluted conditions. For a +10% κ perturbation, the relative change in total N_c under clean conditions (baseline $\kappa = 0.27$) is much lower than that in polluted conditions (baseline $\kappa = 0.45$), ranging from +18.1% to

350 +33.6% (Fig. 10c), with a corresponding decrease in visibility of –10.7% to –16.6% (Fig. 10d). Under clean conditions, these values are +4.2% to +15.0% and –4.4% to –9.7%, respectively.

These results partly support previous studies suggesting that the effect of changes in the chemical composition on the activated number of fog droplets is relatively small compared to the effect of changes in the aerosol size distribution (e.g., Dusek et al., 2006; Mazoyer et al., 2019), particularly under high N_a conditions. However, this does not imply that uncertainties in

355 chemical composition can be neglected when hydrated particles are considered; an accurate representation of κ remains crucial, especially for estimating visibility and fog duration. It is also worthwhile to note that particle composition and size distribution are not decoupled in reality, as both are governed by the sources and atmospheric processing of the emitted particles.

It is also noteworthy that the response of total N_c and the corresponding visibility to κ changes is nonlinear: the sensitivity is much higher for positive κ perturbations than for negative ones. This asymmetry occurs because increasing κ means a

360 higher growth factor, shifting the dry aerosol size spectrum toward larger sizes and allowing more fine particles to exceed the threshold of $2\,\mu m$, which means that they are counted in N_c. Conversely, decreasing κ weakens hygroscopic growth, causing fewer particles to grow beyond the $2\,\mu m$ threshold.
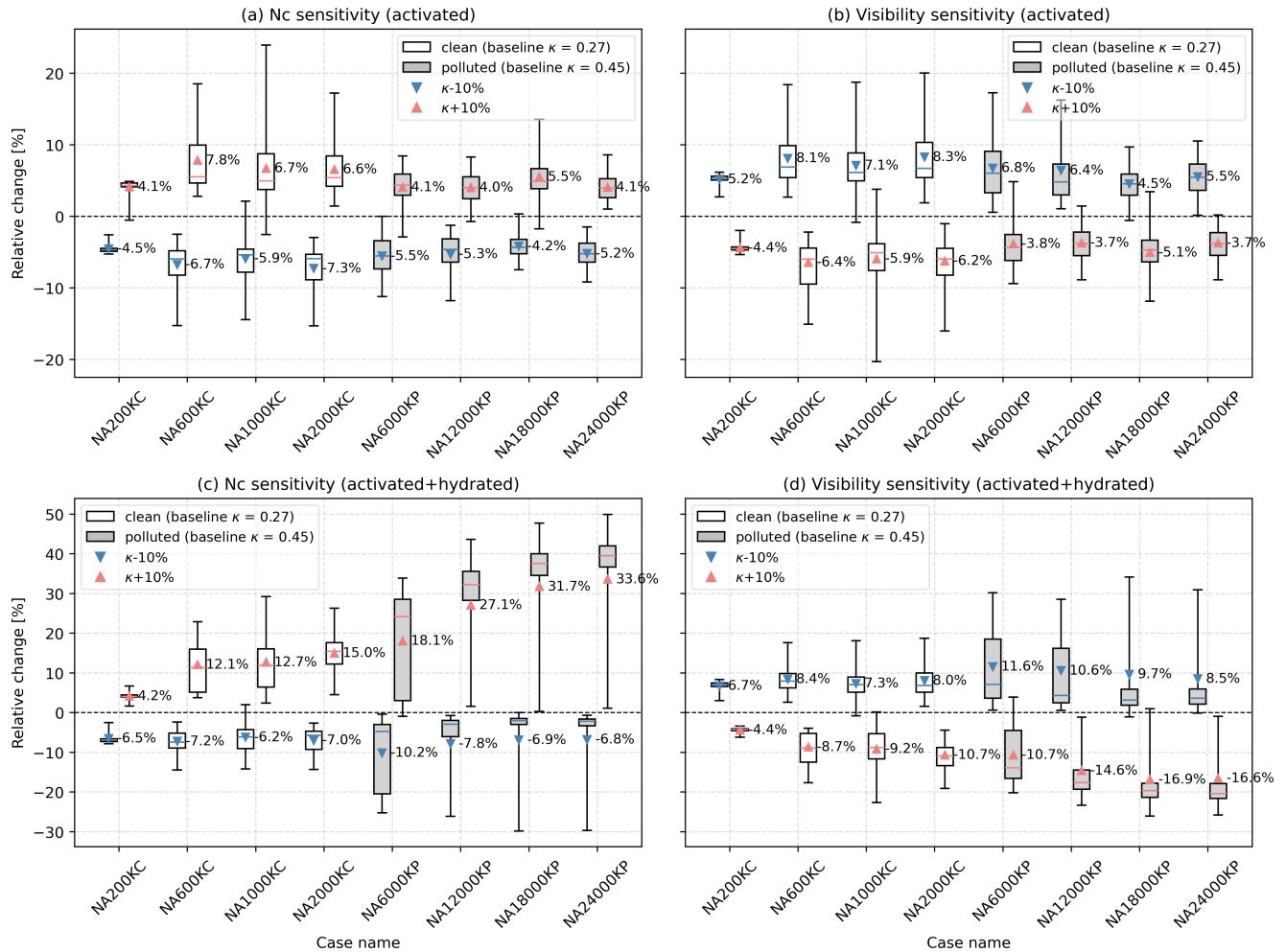
Figure 10. Relative change of fog properties to aerosol hygroscopicity parameter perturbations (blue: κ -10%, red: κ +10%) under different aerosol loading conditions (white box: clean, gray box: polluted), compared with corresponding base κ cases, where (a) the number of activated droplets $N_{c,act}$, (b) visibility parameterized by activated droplets $N_{c,act}$, (c) the number of total droplets N_c (activated + hydrated), and (d) visibility parameterized by total N_c. Boxes represent the 25th–75th percentiles, whiskers the 5th–95th percentiles, solid lines the median, and triangles labeled with numbers indicate the mean.

3.4 Sensitivity to droplet microphysics

As mentioned in Sect. 1 and shown in Fig. 3, the generalized gamma distribution exhibits clear limitations in representing

365 the wide spectrum of fog droplet sizes. For simulations with combinations of small shape parameters, such as [1,1], [1,2], [1,3], and [2,1] (hereafter referred to as wide-spectrum cases), the representation of small droplets is reasonable, but the

number concentration of large droplets (>30 μm) is overestimated, which increases the bulk mean droplet size and consequently enhances the overall sedimentation rate (Fig. 11f). In particular, the average sedimentation velocity in cases DROP_A1N2 and DROP_A1N1 is about 1.6 and 2.0 times higher, respectively, than in the narrow-spectrum cases. Additionally, in these wide-

370 spectrum simulations, liquid water is distributed more evenly across droplet sizes, making the fog liquid water more sensitive to sedimentation losses. Together, these two factors lead to a significant reduction in total N_c and Q_c, and the post-sedimentation droplet population becomes increasingly dominated by hydrated particles (Fig. 12b). Consequently, the mean droplet size is reduced, and near-surface visibility increases (Fig. 11e and g). Fog onset is slightly delayed in the wide-spectrum cases relative to the narrow-spectrum cases, whereas no notable differences are observed among the narrow-spectrum simulations (Fig. 11a).

375 The model does not show a clear correlation between fog dissipation and the prescribed droplet size distribution (Fig. 11b). Also, when increasing N_a under the same wide-spectrum parameter setting, no delay in the fog dissipation similar to that shown in the AERO_NA experiments (Fig. 7b) is observed, suggesting that under enhanced sedimentation regimes, the fog lifetime is less sensitive to N_a (not shown). Furthermore, in the sensitivity experiments with droplet collision–coalescence enabled, no significant differences are observed across the wide-spectrum cases (not shown). This is likely because the fog

380 droplet sizes are generally relatively small, resulting in very low collision–coalescence efficiency and rendering this process negligible for the overall fog properties.

In terms of vertical structure, for wide-spectrum cases, enhanced sedimentation inhibits fog-top lifting and reduces geometric and optical thickness, and the temporal variability in LWP and τ is smoothed out (Fig. 13). In the DROP_A1N1 case, the maximum fog-top height is about 60 m with a mean LWP of 1.57 g m^{-2}, whereas in the narrow-spectrum reference case

385 DROP_A3N1, the maximum fog-top height reaches about 100 m with a mean LWP of 11.87 g m^{-2}.

A comparison among the narrow-spectrum simulations shows that different parameter combinations lead to variations in the fog optical thickness, where a narrower spectrum produces thicker fog layers and some local fluctuations in the near-surface temporal evolution (Fig. 13). Nevertheless, the overall near-surface microphysical statistics – such as droplet number concentration, liquid water content, and the relative fraction of hydrated and activated droplets – show only small differences (Fig. 11

390 and Fig. 12). This indicates that merely adjusting the generalized gamma distribution parameters is insufficient to address the positive bias in activated droplet number concentration and the liquid water content of large droplets.
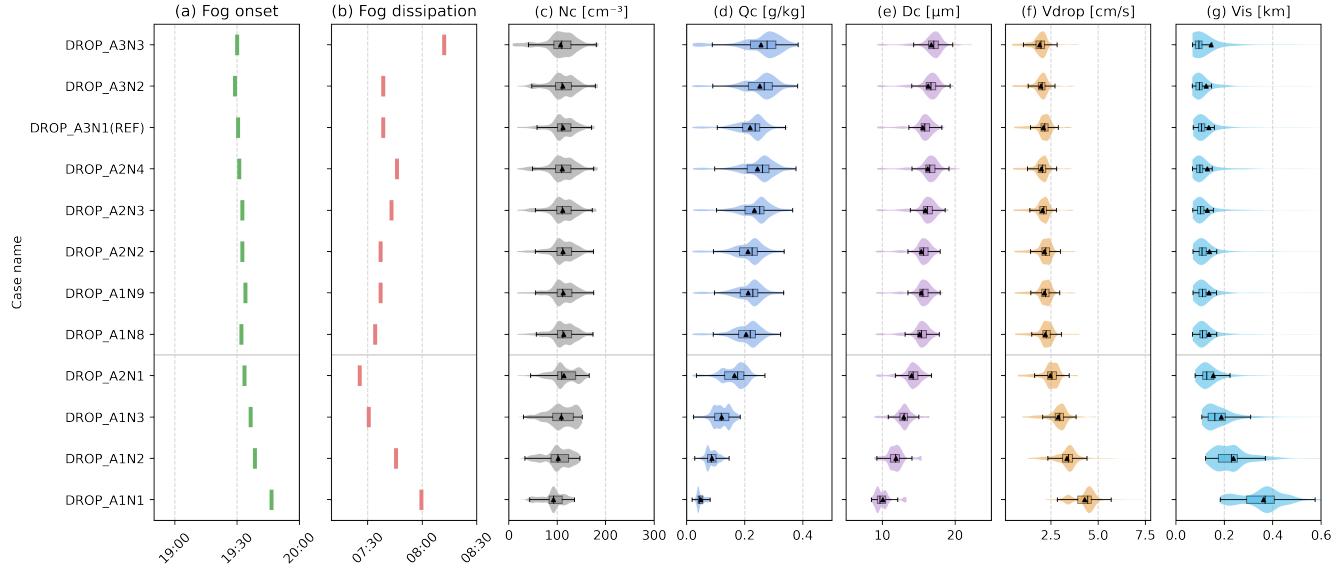
Figure 11. Statistical near-surface fog properties in DROP_AN experiments: (a) fog onset time, (b) fog dissipation time, (c) droplet number concentration N_c, (d) liquid water mixing ratio Q_c, (e) mean droplet diameter D_c, (f) droplet terminal velocity V_{drop} and (g) visibility Vis. Where both activated and hydrated particles are counted in the droplet category. The boxes represent the 25th–75th percentiles, whiskers the 5th–95th percentiles, the solid line the median, and the black triangle the mean. Shaded areas illustrate the distribution of values. Below the dashed line are narrow-droplet-spectrum cases.
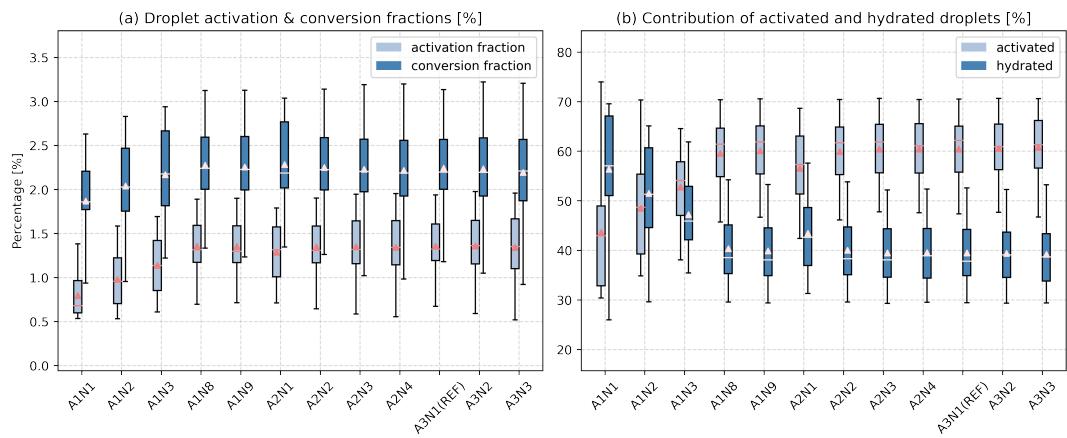
Figure 12. N_c-related statistical results in DROP_AN experiments: (a) droplet activation and conversion fraction, (b) contribution of activated and hydrated particles in total N_c, where light blue boxes represent activated particles, and dark blue ones represent hydrated particles.
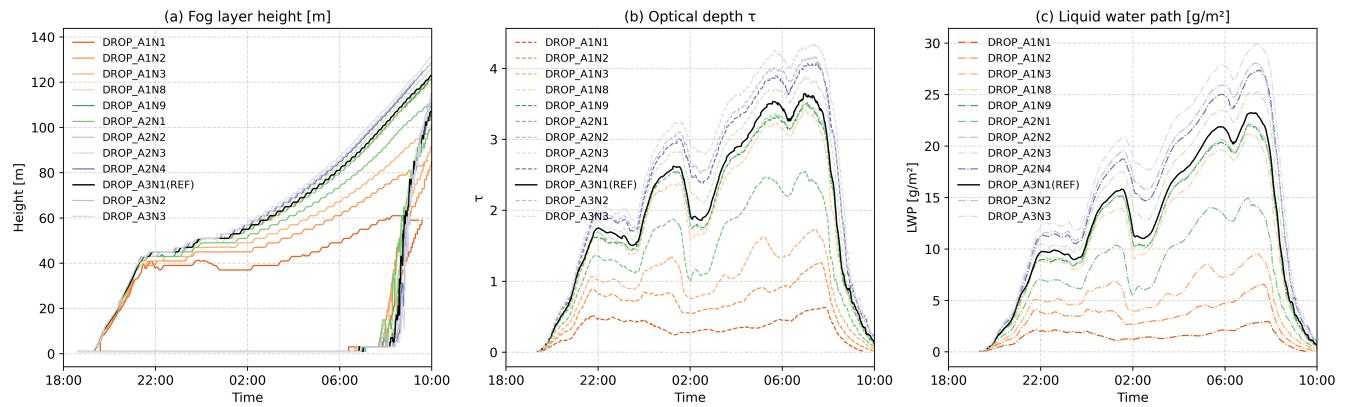
Figure 13. Vertical fog properties in DROP_AN experiments: (a) fog layer height, (b) optical thickness, and (c) liquid water path.

4 Summary and conclusions

Using one-at-a-time sensitivity experiments with prescribed surface forcing and excluding aerosol-radiation interactions, this study isolates and examines cloud microphysical impacts of aerosols and fog droplets on an observed case of wintertime

395 radiation fog in the Po Valley. The results show that an increase in aerosol number concentration generally increases the number of fog droplets, thereby increasing the fog liquid water content, enhancing optical thickness, and reducing visibility. Concurrently, a decrease in the average droplet size weakens sedimentation rates, extending the residence time of droplets and prolonging fog duration by up to 54 minutes. However, these responses are nonlinear; under high-pollution conditions (i.e., in a supersaturation-limited regime), and when only the effects of aerosols as CCN are considered (i.e. no aerosol-radiation

400 interactions), the sensitivity of fog properties and duration to aerosol number is significantly reduced. Moreover, with higher aerosol loading, the droplet activation fraction decreases, and at $N_a > 10{,}000\,\mathrm{cm}^{-3}$, the fog is dominated by hydrated aerosols (haze) rather than activated aerosols (fog droplets). Overall, hydrated aerosols contribute about 40% (REF) to 63% ($N_a = 24{,}000\,\mathrm{cm}^{-3}$) to the total droplet number.

The chemical composition of the aerosol affects the activation of droplets and the hygroscopic growth of the aerosol mainly

405 through the hygroscopicity parameter κ. Compared with the aerosol size distribution, the influence of κ on droplet activation is relatively weak and is, in agreement with previous studies, more pronounced under clean conditions than under polluted conditions. Nevertheless, when hydrated particles are considered, variations in aerosol chemical composition and κ substantially influence the total droplet number concentration and visibility. This underscores the importance of accurately representing aerosol chemical composition and accounting for hydrated aerosol particles in visibility prediction and fog forecasting.

410 For the simulated range of aerosol number concentrations (N_a = 2,000-24,000 cm^{-3}), the fog droplet budget is primarily governed by sedimentation, condensation/evaporation, and turbulent diffusion, whereas autoconversion and collision–coalescence processes play a minor role. With a careful selection of shape parameters, the generalized gamma distribution represents the observed mean size spectrum of activated droplets reasonably. However, employing different parameter combinations found

in the literature, where some produce excessively broad size spectra compared to the observations for the specific case, leads
in some cases to substantial underestimation of the fog droplet number, liquid water content, as well as geometric and optical
thickness. Furthermore, the observed droplet spectrum, which includes hydrated particles, often exhibits multimodal structures.
Given the highlighted importance of hydrated particles, future parameterization schemes could explicitly distinguish between
hydrated particles and activated fog droplet populations and allow for multimodal size distributions to better capture key micro-
physical processes. It is also noteworthy that the bulk microphysics scheme based on κ–Köhler theory tends to underestimate
the hygroscopic growth factor and the number of hydrated particles. Introducing appropriate correction factors based on bin
sizes may improve the representation of aerosol hygroscopic growth.

Overall, this study offers a preliminary framework for understanding the microphysical impacts of aerosols and droplets on fog
evolution. Our future work will incorporate aerosol–radiation–surface interactions to evaluate radiative effects of aerosols, and
their coupled effects with microphysical processes and surface energy balance on radiation fog properties and life cycle.

Acronyms

CCN Cloud Condensation Nuclei

ED Effective Diameter

FAIRARI Fog and Aerosol Interaction Research Italy

LES Large Eddy Simulation

LST Local Standard Time

LWC Liquid Water Content

LWP Liquid Water Path

MIMICA MISU–MIT Cloud and Aerosol model

OAT One-At-a-Time

REF Reference simulation

RH Relative Humidity

SPC San Pietro Capofiume

SSM Surface Skin Moisture

SST Surface Skin Temperature

TKE Turbulence Kinetic Energy

Vis Visibility

Code and data availability. The sounding data for San Pietro Capofium are provided by the University of Wyoming Atmospheric Science Radiosonde Archive (https://weather.uwyo.edu/upperair/sounding.shtml). Aerosol data from the FAIRARI campaign are available through the Data Center of the Bolin Center for Climate Research (https://bolin.su.se/data/fairari-2021-2022). The MIMICA model code can be
445 accessed at (https://bitbucket.org/matthiasbrakebusch/mimicav5/src/master).

Competing interests. Some authors are members of the editorial board of journal Atmospheric Chemistry and Physics.

Acknowledgements. Financial support from the European Union's Horizon 2020 research and innovation programme (Project FORCeS under Grant Agreement 821205), European Research Council (Consolidator Grant INTEGRATE 865799) and Horizon Europe programme (Project CERTAINTY under Grant Agreement 101137680) is gratefully acknowledged. We also acknowledge financial support from the
450 Knut and Alice Wallenberg Foundation through grants for project AtmoRemove (No. 2015.0162), AtmoCLOUD (No. 2021.0169 and No. 2021.0298), and CLIVE (No. 2022.0104), as well as from Goran Gustafssons stiftelse and the Swedish Research Council (No. 2020–04158). The computations and data handling in MIMICA were enabled by resources provided by the National Academic Infrastructure for Supercomputing in Sweden (NAISS), partially funded by the Swedish Research Council (No. 2022-06725).

References

455   Albrecht, B. A.: Aerosols, cloud microphysics, and fractional cloudiness, Science, 245, 1227–1230, 1989.

Alduchov, O. A. and Eskridge, R. E.: Improved Magnus form approximation of saturation vapor pressure, Journal of Applied Meteorology (1988-2005), pp. 601–609, 1996.

Bari, D., Bergot, T., and El Khlifi, M.: Numerical study of a coastal fog event over Casablanca, Morocco, Quarterly Journal of the Royal Meteorological Society, 141, 1894–1905, 2015.

460   Bergot, T.: Small-scale structure of radiation fog: a large-eddy simulation study, Quarterly Journal of the Royal Meteorological Society, 139, 1099–1112, 2013.

Bergot, T. and Koracin, D.: Observation, simulation and predictability of fog: Review and perspectives, Atmosphere, 12, 235, 2021.

Bott, A.: On the influence of the physico-chemical properties of aerosols on the life cycle of radiation fogs, Boundary-Layer Meteorology, 56, 1–31, 1991.

465   Bott, A., Sievers, U., and Zdunkowski, W.: A radiation fog model with a detailed treatment of the interaction between radiative transfer and fog microphysics, Journal of Atmospheric Sciences, 47, 2153–2166, 1990.

Boutle, I., Price, J., Kudzotsa, I., Kokkola, H., and Romakkaniemi, S.: Aerosol–fog interaction and the transition to well-mixed radiation fog, Atmospheric Chemistry and Physics, 18, 7827–7840, 2018.

Boutle, I., Angevine, W., Bao, J.-W., Bergot, T., Bhattacharya, R., Bott, A., Ducongé, L., Forbes, R., Goecke, T., Grell, E., et al.: Demistify:
470   a large-eddy simulation (LES) and single-column model (SCM) intercomparison of radiation fog, Atmospheric Chemistry and Physics, 22, 319–333, 2022.

Brenguier, J.-L., Burnet, F., and Geoffroy, O.: Cloud optical thickness and liquid water path–does the k coefficient vary with droplet concentration?, Atmospheric Chemistry and Physics, 11, 9771–9786, 2011.

Contreras Osorio, S., Martín Pérez, D., Ivarsson, K.-I., Nielsen, K. P., de Rooy, W. C., Gleeson, E., and McAufield, E.: Impact of the
475   Microphysics in HARMONIE-AROME on Fog, Atmosphere, 13, 2127, 2022.

Decesari, S., Sowlat, M. H., Hasheminassab, S., Sandrini, S., Gilardoni, S., Facchini, M. C., Fuzzi, S., and Sioutas, C.: Enhanced toxicity of aerosol in fog conditions in the Po Valley, Italy, Atmospheric Chemistry and Physics, 17, 7721–7731, 2017.

Dimitrelos, A., Ekman, A. M., Caballero, R., and Savre, J.: A sensitivity study of Arctic air-mass transformation using large Eddy simulation, Journal of Geophysical Research: Atmospheres, 125, e2019JD031 738, 2020.

480   Dusek, U., Frank, G., Hildebrandt, L., Curtius, J., Schneider, J., Walter, S., Chand, D., Drewnick, F., Hings, S., Jung, D., et al.: Size matters more than chemistry for cloud-nucleating ability of aerosol particles, Science, 312, 1375–1378, 2006.

Ekman, A. M., Wang, C., Ström, J., and Krejci, R.: Explicit simulation of aerosol physics in a cloud-resolving model: Aerosol transport and processing in the free troposphere, Journal of the atmospheric sciences, 63, 682–696, 2006.

Elias, T., Haeffelin, M., Drobinski, P., Gomes, L., Rangognio, J., Bergot, T., Chazette, P., Raut, J.-C., and Colomb, M.: Particulate contribution
485   to extinction of visible radiation: Pollution, haze, and fog, Atmospheric Research, 92, 443–454, 2009.

Elias, T., Dupont, J.-C., Hammer, E., Hoyle, C., Haeffelin, M., Burnet, F., and Jolivet, D.: Enhanced extinction of visible radiation due to hydrated aerosols in mist and fog, Atmospheric Chemistry and Physics, 15, 6605–6623, 2015.

Frank, G., Martinsson, B. G., Cederfelt, S.-I., Berg, O. H., Swietlicki, E., Wendisch, M., Yuskiewicz, B., Heintzenberg, J., Wiedensohler, A., Orsini, D., et al.: Droplet formation and growth in polluted fogs, Contributions to Atmospheric Physics, 71, 1998.

490 Fuzzi, S., Facchini, M. C., Orsi, G., Lind, J. A., Wobrock, W., Kessel, M., Maser, R., Jaeschke, W., Enderle, K. H., Arends, B. G., Berner, A., Solly, I., Kruisz, C., Reischl, G., Pahl, S., Kaminski, U., Winkler, P., Ogren, J. A., Noone, K. J., Hallberg, A., Fierlinger-Oberlinninger, H., Puxbaum, H., Marzorati, A., Hansson, H.-C., Wiedensohler, A., Svenningsson, I. B., Martinsson, B. G., Schell, D., and Georgii, H. W.: The Po Valley Fog Experiment 1989, Tellus B, 44, 448–468, https://doi.org/https://doi.org/10.1034/j.1600-0889.1992.t01-4-00002.x, 1992.

Geoffroy, O., Brenguier, J.-L., and Burnet, F.: Parametric representation of the cloud droplet spectra for LES warm bulk microphysical
495   schemes, Atmospheric Chemistry and Physics, 10, 4835–4848, 2010.

Gultepe, I., Müller, M. D., and Boybeyi, Z.: A new visibility parameterization for warm-fog applications in numerical weather prediction models, Journal of applied meteorology and climatology, 45, 1469–1480, 2006.

Gultepe, I., Tardif, R., Michaelides, S. C., Cermak, J., Bott, A., Bendix, J., Müller, M. D., Pagowski, M., Hansen, B., Ellrod, G., et al.: Fog research: A review of past achievements and future perspectives, Pure and applied geophysics, 164, 1121–1159, 2007.

500 Haeffelin, M., Bergot, T., Elias, T., Tardif, R., Carrer, D., Chazette, P., Colomb, M., Drobinski, P., Dupont, E., Dupont, J.-C., et al.: PARIS-FOG: Shedding new light on fog physical processes, Bulletin of the American Meteorological Society, 91, 767–783, 2010.

Hamed, A., Joutsensaari, J., Mikkonen, S., Sogacheva, L., Dal Maso, M., Kulmala, M., Cavalli, F., Fuzzi, S., Facchini, M. C., Decesari, S., Mircea, M., Lehtinen, K. E. J., and Laaksonen, A.: Nucleation and growth of new particles in Po Valley, Italy, Atmospheric Chemistry and Physics, 7, 355–376, https://doi.org/10.5194/acp-7-355-2007, 2007.

505 Hammer, E., Gysel, M., Roberts, G., Elias, T., Hofer, J., Hoyle, C. R., Bukowiecki, N., Dupont, J.-C., Burnet, F., Baltensperger, U., et al.: Size-dependent particle activation properties in fog during the ParisFog 2012/13 field campaign, Atmospheric Chemistry and Physics, 14, 10 517–10 533, 2014.

Heikkinen, L., Äijälä, M., Riva, M., Luoma, K., Dällenbach, K., Aalto, J., Aalto, P., Aliaga, D., Aurela, M., Keskinen, H., et al.: Long-term sub-micrometer aerosol chemical composition in the boreal forest: inter-and intra-annual variability, Atmospheric Chemistry and Physics,
510   20, 3151–3180, 2020.

Hersbach, H., Bell, B., Berrisford, P., Biavati, G., Horányi, A., Muñoz Sabater, J., Nicolas, J., Peubey, C., Radu, R., Rozum, I., et al.: ERA5 hourly data on pressure levels from 1940 to present, Copernicus climate change service (c3s) climate data store (cds), 10, 24 381, 2023.

Igel, A. L. and van den Heever, S. C.: The importance of the shape of cloud droplet size distributions in shallow cumulus clouds. Part II: Bulk microphysics simulations, Journal of the Atmospheric Sciences, 74, 259–273, 2017.

515 Jia, X., Quan, J., Zheng, Z., Liu, X., Liu, Q., He, H., and Liu, Y.: Impacts of anthropogenic aerosols on fog in North China Plain, Journal of Geophysical Research: Atmospheres, 124, 252–265, 2019.

Kokkola, H., Romakkaniemi, S., and Laaksonen, A.: On the formation of radiation fogs under heavily polluted conditions, Atmospheric chemistry and Physics, 3, 581–589, 2003.

Lakra, K. and Avishek, K.: A review on factors influencing fog formation, classification, forecasting, detection and impacts, Rendiconti
520   Lincei. Scienze Fisiche e Naturali, 33, 319–353, 2022.

Leung, A. C., Gough, W. A., and Butler, K. A.: Changes in fog, ice fog, and low visibility in the Hudson Bay Region: Impacts on aviation, Atmosphere, 11, 186, 2020.

Liou, K.: Parameterization of the radiative properties of cirrus clouds, Journal of the atmospheric sciences, 50, 2008–2025, 1993.

Maalick, Z., Kühn, T., Korhonen, H., Kokkola, H., Laaksonen, A., and Romakkaniemi, S.: Effect of aerosol concentration and absorbing
525   aerosol on the radiation fog life cycle, Atmospheric Environment, 133, 26–33, 2016.

Maronga, B. and Bosveld, F.: Key parameters for the life cycle of nocturnal radiation fog: a comprehensive large-eddy simulation study, Quarterly Journal of the Royal Meteorological Society, 143, 2463–2480, 2017.

Mazoyer, M., Burnet, F., Denjean, C., Roberts, G. C., Haeffelin, M., Dupont, J.-C., and Elias, T.: Experimental study of the aerosol impact on fog microphysics, Atmospheric Chemistry and Physics, 19, 4323–4344, 2019.

530   Mazoyer, M., Burnet, F., and Denjean, C.: Experimental study on the evolution of droplets size distribution during the fog life cycle, Atmospheric Chemistry and Physics Discussions, 2022, 1–28, 2022.

Miles, N. L., Verlinde, J., and Clothiaux, E. E.: Cloud droplet size distributions in low-level stratiform clouds, Journal of the atmospheric sciences, 57, 295–311, 2000.

Morrison, H. and Grabowski, W. W.: Comparison of bulk and bin warm-rain microphysics models using a kinematic framework, Journal of
535   the atmospheric sciences, 64, 2839–2861, 2007.

Morrison, H. and Grabowski, W. W.: Modeling supersaturation and subgrid-scale mixing with two-moment bulk warm microphysics, Journal of the Atmospheric Sciences, 65, 792–812, 2008.

Neuberger, A., Ranjan, R., Ding, H., Mattsson, F., Haberstock, L., Baumgardner, D., Decesari, S., Ekman, A. M., Hughes, D. D., Mohr, C., et al.: Importance of hydrated aerosol particles for aerosol-fog relationships in the Italian Po Valley, EGUsphere[preprint], 2025, 1–38,
540   https://doi.org/10.5194/egusphere-2025-5419, 2025a.

Neuberger, A., Decesari, S., Aktypis, A., Andersen, H., Baumgardner, D., Bianchi, F., Busetto, M., Cai, J., Cermak, J., Dipu, S., et al.: From Molecules to Droplets: The Fog and Aerosol Interaction Research Italy (FAIRARI) 2021/22 Campaign, Bulletin of the American Meteorological Society, 106, E23–E50, 2025b.

Noone, K. J., Ogren, J. A., Hallberg, A., Heintzenberg, J., Strom, J., Hansson, H.-C., Svenningsson, B., Wiedensohler, A., Fuzzi, S., Facchini,
545   M. C., et al.: Changes in aerosol size- and phase distributions due to physical and chemical processes in fog, Tellus B, 44, 489–504, 1992.

Paglione, M., Gilardoni, S., Rinaldi, M., Decesari, S., Zanca, N., Sandrini, S., Giulianelli, L., Bacco, D., Ferrari, S., Poluzzi, V., Scotto, F., Trentini, A., Poulain, L., Herrmann, H., Wiedensohler, A., Canonaco, F., Prévôt, A. S. H., Massoli, P., Carbone, C., Facchini, M. C., and Fuzzi, S.: The impact of biomass burning and aqueous-phase processing on air quality: a multi-year source apportionment study in the Po Valley, Italy, Atmospheric Chemistry and Physics, 20, 1233–1254, https://doi.org/10.5194/acp-20-1233-2020, 2020.

550   Petters, M. and Kreidenweis, S.: A single parameter representation of hygroscopic growth and cloud condensation nucleus activity, Atmospheric Chemistry and Physics, 7, 1961–1971, 2007.

Pope, N. H. and Igel, A. L.: Identifying Important Microphysical Properties and Processes for Marine Fog Forecasts, Monthly Weather Review, 151, 2427–2441, 2023.

Price, J.: Radiation fog. Part I: observations of stability and drop size distributions, Boundary-layer meteorology, 139, 167–191, 2011.

555   Riipinen, I., Talvinen, S., Chassaing, A., Georgakaki, P., Li, X., Pérez Garcia-Pando, C., Bergman, T., Kommula, S., Proske, U., Gkouvousis, A., Tsimpidi, A., Chatziparaschos, M., Neuberger, A., Karydis, V., Calderón, S., Romakkaniemi, S., Partridge, D., Khadir, T., Dada, L., Van Noije, T., Decesari, S., Seland, O., Zieger, P., Bender, F., Carslaw, K., Cermak, J., Costa-Surós, M., Ageitos, M., Gramlich, Y., Haugvaldstad, O., Holopainen, E., Hoose, C., Jorba, O., Kakavas, S., Kanakidou, M., Kokkola, H., Krejci, R., Kühn, T., Kulmala, M., Le Sager, P., Makkonen, R., Manavi, S., Mentel, T., Milousis, A., Myriokefalitakis, S., Nenes, A., Nieminen, T., Pandis, S., Patoulias,
560   D., Petäjä, T., Quaas, J., Regayre, L., Scholz, S., Schulz, M., Skyllakou, K., Sousse, R., Stier, P., Thomas, M., Villinger, J., Virtanen, A., Wyser, K., and Ekman, A.: Treatment of key aerosol and cloud processes in Earth System Models – Recommendations from the FORCeS Project, Tellus B: Chemical and Physical Meteorology, in press, 2025.

Rose, D., Nowak, A., Achtert, P., Wiedensohler, A., Hu, M., Shao, M., Zhang, Y., Andreae, M., and Pöschl, U.: Cloud condensation nuclei in polluted air and biomass burning smoke near the mega-city Guangzhou, China–Part 1: Size-resolved measurements and implications
565   for the modeling of aerosol particle hygroscopicity and CCN activity, Atmospheric Chemistry and Physics, 10, 3365–3383, 2010.

Savre, J., Ekman, A. M. L., and Svensson, G.: Technical note: Introduction to MIMICA, a large-eddy simulation solver for cloudy planetary boundary layers, Journal of Advances in Modeling Earth Systems, 6, 630–649, https://doi.org/https://doi.org/10.1002/2013MS000292, 2014.

Schwarz, M., Savre, J., Sudhakar, D., Quaas, J., and Ekman, A. M.: The Transition from Aerosol-to Updraft-Limited Susceptibility Regime in Large-Eddy Simulations with Bulk Microphysics, Tellus B: Chemical and Physical Meteorology, 76, 2024.

Schwenkel, J. and Maronga, B.: Large-eddy simulation of radiation fog with comprehensive two-moment bulk microphysics: impact of different aerosol activation and condensation parameterizations, Atmospheric Chemistry and Physics, 19, 7165–7181, 2019.

Seifert, A. and Beheng, K. D.: A double-moment parameterization for simulating autoconversion, accretion and selfcollection, Atmospheric research, 59, 265–281, 2001.

Seifert, A. and Beheng, K. D.: A two-moment cloud microphysics parameterization for mixed-phase clouds. Part 1: Model description, Meteorology and atmospheric physics, 92, 45–66, 2006.

Seinfeld, J. H. and Pandis, S. N.: Atmospheric chemistry and physics: from air pollution to climate change, John Wiley & Sons, 2016.

Stolaki, S., Haeffelin, M., Lac, C., Dupont, J.-C., Elias, T., and Masson, V.: Influence of aerosols on the life cycle of a radiation fog event. A numerical and observational study, Atmospheric Research, 151, 146–161, 2015.

Stull, R. B.: An Introduction to Boundary Layer Meteorology, Kluwer Academic Publishers, Dordrecht, 1988.

Twomey, S.: The influence of pollution on the shortwave albedo of clouds, Journal of Atmospheric Sciences, 34, 1149–1152, 1977.

Wainwright, C., Chang, R. Y.-W., and Richter, D.: Aerosol activation in radiation fog at the atmospheric radiation program Southern Great Plains site, Journal of Geophysical Research: Atmospheres, 126, e2021JD035 358, 2021.

Wobrock, W., Schell, D., Maser, R., Kessel, M., Jaeschke, W., Fuzzi, S., Facchini, M., Orsi, G., Marzorati, A., Winkler, P., et al.: Meteorological characteristics of the Po Valley fog, Tellus B, 44, 469–488, 1992.

Wurtz, J., Bouniol, D., Vié, B., and Lac, C.: Evaluation of the AROME model's ability to represent ice crystal icing using in situ observations from the HAIC 2015 field campaign, Quarterly Journal of the Royal Meteorological Society, 147, 2796–2817, 2021.

Yan, S., Zhu, B., Huang, Y., Zhu, J., Kang, H., Lu, C., and Zhu, T.: To what extents do urbanization and air pollution affect fog?, Atmospheric Chemistry and Physics, 20, 5559–5572, 2020.

Yan, S., Zhu, B., Zhu, T., Shi, C., Liu, D., Kang, H., Lu, W., and Lu, C.: The effect of aerosols on fog lifetime: Observational evidence and model simulations, Geophysical Research Letters, 48, e2020GL61 803, 2021.

Zhang, X., Musson-Genon, L., Dupont, E., Milliez, M., and Carissimo, B.: On the influence of a simple microphysics parametrization on radiation fog modelling: A case study during parisfog, Boundary-layer meteorology, 151, 293–315, 2014.